Materials Science & Engineering A 885 (2023) 145591

Contents lists available at ScienceDirect

Materials Science & Engineering A

journal homepage: www.elsevier.com/locate/msea

Enhancement of strength in laser-joined Al-TRIP and Si-TRIP steels: Microstructural insights and deformation analysis

Atef Hamada [a,*], Ali Khosravifard [b], Sumit Ghosh [c], Matias Jaskari [a], Marion Kreins [d], Walaa Abd-Elaziem [e], Mohamed Wahba [f], Essam Ahmed [g], Tarek Allam [g,h]

[a] Kerttu Saalasti Institute, Future Manufacturing Technologies, University of Oulu, Pajatie 5, FI-85500, Nivala, Finland
[b] Department of Materials and Metallurgical Engineering, Abadeh Higher Education Center, Shiraz University, Abadeh, 73916, Iran
[c] Materials and Mechanical Engineering, Centre for Advanced Steels Research, University of Oulu, FI-90014, Finland
[d] Steel Institute, RWTH Aachen University, Intzestraße 1, 52072, Aachen, Germany
[e] Department of Mechanical Design and Production Engineering, Faculty of Engineering, Zagazig University, P.O. Box 44519, Egypt
[f] Central Metallurgical Research & Development Institute (CMRDI), Helwan, 11421, Egypt
[g] Department of Metallurgical and Materials Engineering, Suez University, 43528, Suez, Egypt
[h] Institute of Energy and Climate Research: Structure and Function of Materials (IEK-2), Forschungszentrum Jülich GmbH, 52425, Jülich, Germany

ARTICLE INFO

Keywords:
TRIP steel
Laser welding
Mechanical properties
Microstructure
Strengthening mechanisms
Finite element simulation

ABSTRACT

This study highlights the strengthening mechanisms observed during the metal joining of high-strength grade steels (Al-TRIP and Si-TRIP) by providing a concise investigation of microstructural features, mechanical strength evaluation, and employing Finite Element Method (FEM) analysis to understand the deformation behaviour in the joint. The base metals (BMs), Al-TRIP and Si-TRIP are cold-rolled sheets with thicknesses of 0.9 mm and 1.3 mm, respectively. Al-TRIP contains 2.4 wt% Al, while Si-TRIP contains 1.5 wt% Si. The Al-/Si-TRIP joint was processed by laser welding at low energy input 24 J/mm. Electron backscattering diffraction and transmission electron microscopy extensively characterized the microstructural features in the fusion zone (FZ) and heat-affected zone (HAZ) to study strengthening mechanisms induced by welding. Uniaxial tensile tests examined joint mechanical strength, while microindentation hardness (H_{IT}) measurements evaluated mechanical response in the weld zones. The FZ showed a fully martensitic structure, while the HAZs displayed refined grains. Ultrafine-grained structures with an average size of 1 μm were observed in the HAZs, resulting in higher H_{IT} hardness values (~6.7 GPa) compared to the FZ (~6.3 GPa). Interestingly, the mechanical tensile properties of the joint were unaffected as failure occurred in the thinner Al-TRIP steel. Finite Element Method (FEM) analysis simulated the tensile testing, revealing localized plasticity in the thinner Al-TRIP and explaining the observed fracture.

1. Introduction

In recent years, the automotive industry has been focused on achieving two primary objectives: reducing greenhouse gas (GHG) emissions to create a cleaner environment and simultaneously enhancing the crashworthiness performance of lightweight vehicles [1,2]. To meet these goals, it is necessary to utilize bodywork steels with ultrahigh strength. Among the potential advanced high-strength steel grades for the automotive industry, transformation-induced plasticity (TRIP) steels with low-alloying elements have garnered attention due to their ability to offer both high energy absorption for crashworthiness and lightweight material properties. TRIP steel is commonly used in assembling car bodies, specifically the body-in-white [3]. Previous studies have reported that TRIP steel exhibits superior mechanical properties, including an ultimate tensile strength (UTS) range of 500–1000 MPa, good formability with uniform elongation ranging from 20% to 40%, and high dynamic energy absorption during high-strain-rate crash deformation [4,5].

De Cooman [6] emphasized that TRIP-aided steels demonstrate excellent deep drawability and stretch formability properties comparable to those of low carbon steels. Consequently, TRIP steels are well-suited for demanding automotive applications, often utilized in constructing B-pillars and absorption boxes [7]. Consequently, researchers have shown interest in studying the weldability of TRIP steels

* Corresponding author.
E-mail addresses: atef.hamadasaleh@oulu.fi, atef.hamada@gmail.com (A. Hamada).

https://doi.org/10.1016/j.msea.2023.145591
Received 12 July 2023; Received in revised form 13 August 2023; Accepted 19 August 2023
Available online 22 August 2023

for metal joining. According to the Steel Weldability Diagram, such as the Granville weldability graph, specific welding procedures must be employed to prevent cold cracks during the welding process [6]. The addition of silicon (Si) and aluminium (Al) to TRIP steels is known to have a significant impact on their mechanical properties and industrial feasibility.

The application of laser welding in the study of TRIP (Transformation Induced Plasticity) steels has gained significant attention in recent research. Several investigations have explored the defects, microstructure, mechanical properties, and formability of laser-welded TRIP steels, focusing on different grades and alloy compositions.

Xia et al. [8] conducted a study on laser-welded TRIP steels alloyed with Al and Si, focusing on the microstructure and mechanical properties. They observed that the fusion zone (FZ) of Si-alloyed steel exhibited a greater reduction in the strength-ductility balance compared to the Al-alloyed steel in both quasi-static and dynamic tensile tests. Subsequently, the same authors investigated the microstructure evolution, solidification mode, and solid-state transformation of Al-alloyed TRIP steel during laser welding [9]. Their findings indicated that the FZ microstructure primarily consisted of upper bainite and skeletal morphology ferrite, accounting for approximately 35% of the structure.

In a related study, Guzman-Aguilera et al. [10] utilized different welding techniques, including laser beam welding (LBW) and two arc welding processes, namely gas tungsten arc welding (GTAW) and gas metal arc welding (GMAW), to explore the impact of net heat input on the microstructure, tensile properties, and formability of Si-alloyed TRIP steel. Their investigation revealed that the extent of softening and ductility was influenced by the specific welding technique employed. LBW demonstrated the most favourable outcomes, effectively reducing softening and minimizing the overall size of the FZ and the heat affected zone (HAZ). Han et al. [11] examined the weld characteristics of grade 800 MPa TRIP steel welded using a CO2 laser. The weld exhibited a dual-phase microstructure of martensite-ferrite. Tensile testing revealed that the joint fractured in the base metal (BM), indicating the weld's superior strength compared to the BM. Zhang et al. [12] studied the microstructure, tensile properties, and formability of laser-welded 1.2 GPa grade hot-rolled TRIP steel with 1.7 wt% Si. The FZ exhibited full martensite, displaying higher hardness than the BM. The TRIP joint achieved a remarkable efficiency of 96.6% compared to the BM. Wang et al. [13] investigated the laser-welded joints of cold-rolled TRIP steel sheets with Al and Si contents of approximately 0.9 wt% and 1 wt%, respectively. The FZ exhibited a microstructure comprising lath martensite and lower bainite. Tensile testing demonstrated discontinuous yielding behaviour similar to that of the BM, and joint failure occurred in the BM with identical ultimate tensile strength values. Nayak et al. [14] explored the microstructure evolution and hardness of alloyed TRIP steels during resistance spot welding, considering different alloy compositions. Furthermore, researchers have employed advanced laser welding techniques such as twin-spot laser welding [15]. Lang et al. [16] applied hybrid low-power laser-TIG arc welding for processing lap joints of TRIP steels.

Many studies stated the assessment of laser welding of dissimilar welded joints between TRIP steel and different high-strength grade steels. Laser welding could achieve high-quality dissimilar welded joints applying wide range of parameters [17]. For instance, Wu et al. [18] processed dissimilar butt joints between TRIP780 steel and QP1180 steel sheets with different thicknesses by fiber laser welding to study the microstructure evolution, mechanical properties, and formability. Sharma and Molian [19] processed dissimilar joints between 1 mm thick TRIP sheet steel 780 MPa grade and cold-rolled sheets of 1.5 mm thick DP980 and 1 mm thick mild C-steel, separately, by laser welding. High-quality dissimilar joints, TRIP780/DP980 and TRIP780/C-steel, with excellent strength and hardness were obtained by laser welding.

Mujica et al. [20] examined the feasibility of laser-welded joints between low-alloyed TRIP steel and high-Mn twinning-induced plasticity (TWIP) steel sheets. They observed a predominantly austenitic microstructure in the FZ, with small martensitic regions acting as crack initiation sites during tensile testing.

In the automotive industry, laser tailor-welded blank assembly of multi-thickness steel sheets is commonly employed to reinforce A- and B-pillars and door rings, reducing weight and cost while improving crash performance [21,22]. Kohar et al. [23] proposed a constitutive model aimed at assessing the crashworthiness of spot-welded TRIP 800 steel. By simulating the thermo-mechanical behaviour, the model enables the prediction of energy absorption characteristics during axial crush loading, providing valuable insights into the material's crash performance.

In previous studies, considerable attention has been given to investigating the effects of Si and Al additions in TRIP steels, primarily in relation to their microstructure, mechanical properties, and weldability. However, there remains a significant research gap regarding the understanding of the strengthening mechanisms and mechanical behaviour specifically in laser-welded TRIP steels with high Al and Si content.

Addressing this research gap, our study takes a step forward by fabricating laser-welded joints using thin cold-rolled TRIP steel sheets with elevated Al and Si contents, employing a low energy input of 24 J/mm.

Cold-rolled thin sheets of TRIP steels have gained recognition as highly promising Ultra-High-Strength Steel (UHSS) materials within the automotive industry, serving to simultaneously enhance strength and reduce the weight of vehicles. In the manufacturing of the body-in-white (BIW), metal laser welding is commonly employed to join different sheets together. In this study, our objective was to investigate the effect of severe plastic deformation on the microstructural characteristics and subsequent deformation behavior of laser-joined Al-TRIP and Si-TRIP steels. By focusing on these laser-welded TRIP joints, we aimed to evaluate the influence of cold rolling on the underlying mechanisms responsible for strength enhancement and the overall performance of the joint.

To comprehensively investigate the strengthening mechanisms in the FZ and HAZ, we employ a multi-faceted approach. Firstly, we employ advanced characterization techniques such as electron backscattered diffraction (EBSD) and transmission electron microscopy (TEM) to analyze and understand the microstructural aspects. Secondly, we evaluate the mechanical response through microindentation hardness (H_{IT}) measurements, providing insights into the material's local strength characteristics.

In addition to the experimental investigation, we integrate the obtained mechanical results into a finite element model. This allows us to assess the influence of sheet thickness differences on the plasticity of the paired Al-TRIP and Si-TRIP materials, providing a comprehensive understanding of the mechanical behaviour under various conditions.

By combining these approaches, our study offers a novel and comprehensive analysis of the weld-induced microstructural features, strengthening mechanisms, and mechanical behaviour of laser-welded TRIP steels with high Al and Si content. Our findings contribute to advancing the understanding of these complex materials and pave the way for optimized welding strategies and enhanced performance in practical applications.

2. Experimental procedures

2.1. Materials

In this study, the experimental materials, BMs, are TRIP steels bearing various alloying elements of Al and Si. The BMs sheets were delivered by ThyssenKrupp Steel Europe AG (TKSE), Germany, in the form of cold-rolled sheets with various thicknesses of 0.9 and 1.3 mm. The chemical compositions of the BMs are illustrated in Table 1.

Table 1
Chemical compositions of BMs, Al-TRIP and Si-TRIP.

Steel code	Thick, mm	C	Mn	Si	Al	Fe
Al-TRIP	0.9	0.26	1.66	0.14	2.43	Bal.
Si-TRIP	1.3	0.25	1.48	1.5	0.06	Bal.

2.2. Laser welding setup

The butt joints between the BMs (Al-TRIP and Si-TRIP) were laser-welded using a continuous-wave disc laser machine (Trumpf-TruDisk 16002) with a power output of 16 kW. The welding process was conducted with specific parameters set as follows: a focal length of 300 mm, a defocusing distance of −5 mm to achieve a laser beam spot diameter of 0.3 mm, a welding speed of 5 m/min, and a laser power of 2 kW. During welding, the laser beam was angled at 10° to the paired metals. The calculated energy input in the joint was 24 J m^{-1}. To ensure optimal welding conditions, the laser beam was offset by 0.15 mm towards the thicker sheet. A shielding gas of pure argon was employed, with a flow rate of 30 l min^{-1}, directed through a coaxial nozzle at an angle of 40° to the paired metals. A schematic diagram of the laser welding setup can be seen in Fig. 1. To prevent distortion and movement of the samples during laser welding, a special fixture was utilized to firmly clamp the paired metals onto the base plate.

2.3. Microstructural characterization & mechanical tests

The microstructural features of the FZ and HAZs adjacent to the BMs were extensively investigated using EBSD technique integrated into a field-emission gun scanning electron microscope (FEG-SEM) (Model: JEOL JSM-7900F). For the metallographic examination, the TRIP weldment was sectioned perpendicular to the welding direction, and the transverse cross-section underwent standard preparation techniques. This involved mechanical polishing using SiC papers, followed by further polishing down to 1 μm using a diamond suspension. The specimens were then chemically polished with a 0.05 μm colloidal suspension of silica for approximately 10 min. EBSD mapping was performed with specific operational parameters, including an accelerating voltage of 15 kV, a working distance of 12 mm, and different fine step sizes of 0.1 μm and 0.5 μm for high and low magnification maps, respectively.

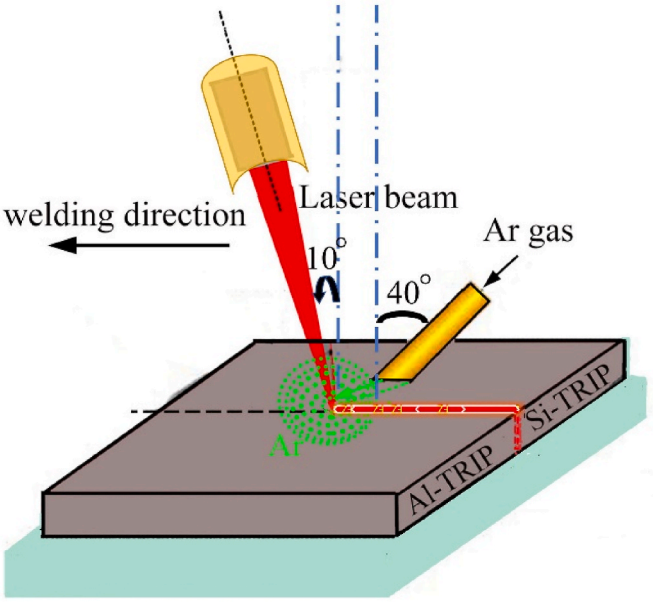

Fig. 1. Schematic representation of the laser welding process for TRIP steels, illustrating the welding setup.

To investigate the nanoscale features of the microstructures, TEM was employed using a JEOL 2200FS instrument. Thin lamellas were prepared from the specimens using the focused ion beam (FIB) technique to enable subsequent TEM analysis. The TEM operated at 200 kV, providing high-resolution imaging capabilities to examine the evolution and coexistence of various phases and precipitates. Selected area electron diffraction (SAD) patterns were recorded and analysed to identify the corresponding phases and precipitates.

The mechanical strength of the TRIP joint was assessed through uniaxial tensile testing conducted at a strain rate of 10^{-3} s^{-1}. Tensile testing specimens were prepared from the weldments following the ASTM-E8 standard, with the following dimensions: a gage length of 70 mm, a width of 12.5 mm, and a total length of 200 mm. Three samples were tested for each condition. Additionally, to provide a basis for comparison, the BMs were also subjected to tensile testing at the same strain rate.

H_{IT} measurements were performed on both the weldment and the BMs to examine the mechanical response of the different zones within the weld. An instrumented indentation tester (CSM Instruments, United States) equipped with a diamond Berkovich indenter was utilized for the H_{IT} measurements. The H_{IT} tests involved applying an indentation load and analysing the resulting penetration depth, as well as the loading-unloading curves, to characterize the mechanical behaviour of each weld zone [24]. The H_{IT} tests were conducted by gradually ramping up the load until reaching a maximum of 3 N.

2.4. Finite element modelling (FEM)

The FEA methodology provided a valuable tool for understanding the structural response of the dissimilar welded joint, allowing for the investigation of stress and deformation patterns, and aiding in the interpretation of the experimental results. In order to investigate the stress and deformation distribution during uniaxial tensile testing of the dissimilar TRIP welded sample, a comprehensive FE model was developed using the ANSYS 19 software package. The model accurately represented the geometry of the experimental sample, where the 0.9 mm thick Al-TRIP part was joined to the 1.3 mm thick Si-TRIP strip.

The FEA model consisted of a three-dimensional representation of the tensile specimen, as depicted in Fig. 2. Each side of the model was divided into three distinct volumes, representing the BMs, HAZ), and FZ. To account for the material behaviour, bilinear rate-independent isotropic hardening was applied to both the Al-TRIP and Si-TRIP materials, considering their limited plasticity and similar yield and ultimate

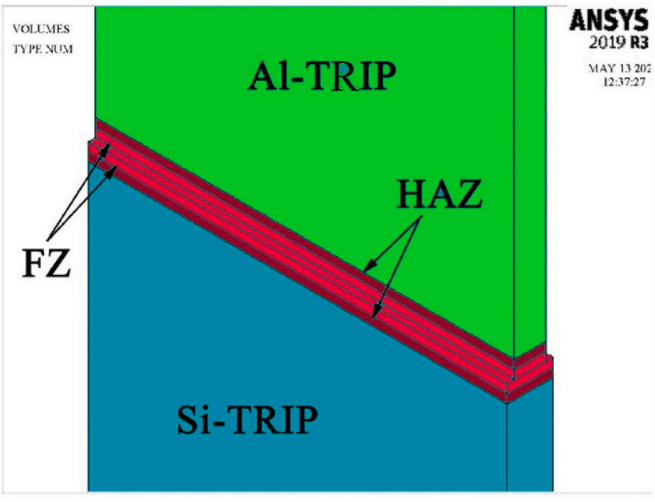

Fig. 2. Finite element model created to simulate the tensile test of the dissimilar laser-welded Al-TRIP/Si-TRIP joint.

strengths. The material properties for the HAZ and FZ volumes were estimated based on the available hardness test data. These properties were incorporated into the model to accurately capture the mechanical response of the respective zones. The six volumes within the model were connected through gluing interfaces to ensure proper interaction and continuity.

Boundary conditions were applied to simulate the uniaxial tensile loading. The grip region of the Si-TRIP side was fully fixed in all directions to restrict its movement. On the other hand, the grip region of the Al-TRIP side was subjected to a uniaxial stretching load, representing the tensile loading condition. A meshing process was performed on the model, resulting in a total of 33,755 solid 186 three-dimensional elements. This mesh discretization allowed for an accurate representation of the specimen's geometry and facilitated the analysis of stress and deformation distribution. The resulting stress and deformation distributions were analysed to gain insights into the mechanical behaviour and load transfer mechanisms within the dissimilar welded joint during uniaxial tensile testing.

3. Results & discussion

3.1. Microstructure characteristics revealed by EBSD examination

TRIP steels with Al and Si additions are known for their complex multiphase microstructures. The thermomechanical processing of these steels typically results in a microstructure consisting of ferrite matrix, acicular martensite/bainite components, and approximately 10% retained austenite [25,26]. Our EBSD examination provided valuable insights into the microstructural characteristics of the experimental TRIP steels and highlighted the influence of cold deformation on their multiphase nature. The experimental BMs, Al-TRIP, and Si-TRIP underwent severe cold deformation to achieve thin sheets. The microstructural features of the BMs are depicted in Fig. 3. The images obtained from the Image Quality (IQ) maps in Fig. 3(a) and (b) reveal heavily deformed microstructures characterized by elongated/stretched grains, forming a pancake-like grain structure. Additionally, certain zones colored black in the images could not be indexed by EBSD due to the extensive cold-rolling deformation, which induces highly localized deformation bands with a high density of dislocations. The presence of these dislocated structures impedes the indexing of phases by EBSD due to the significant stored strain energy [27]. The corresponding phase maps, shown in Fig. 3(c) and (d), display a unified phase colored in red, which can be identified as ferrite or martensite. It is well-documented that the α′-bct crystal structure of the martensite phase and the α-bcc crystal structure of ferrite can be indexed as bcc-cubic crystals in EBSD mapping [28]. However, distinguishing between martensite and ferrite based on morphology is possible. The ferrite grains, indicated by the letter "F" in Fig. 3(d), appear as wide elongated grains. The fine grains located at the boundaries of the ferrite grains may consist of other phase components, such as martensite, bainite, or retained austenite transformed into martensite during the cold-rolling deformation.

For industrial purposes, the Al- and Si-TRIP steels underwent significant reductions in thickness during the cold rolling process, specifically around 75% and 60% reduction of true deformation strains, corresponding to 1.4 and 0.9, respectively. Fig. 3 provides clear evidence of the resulting microstructures, where the Al-TRIP steel exhibits a narrower width of the pancake-like structure compared to Si-TRIP steel, owing to the higher level of cold deformation. As a result, both Al-TRIP and Si-TRIP demonstrate superior mechanical strength while maintaining a slight elongation capability. The mechanical properties will be discussed in Section 3.3.

Microstructure characteristics of laser-welded TRIP steels were investigated, and a comprehensive analysis is presented in Fig. 4. The IQ map in Fig. 4(a) reveals distinct differences in the grain structure morphology between FZ, BMs, and HAZs. Specifically, columnar grains are observed in the FZ, which can be attributed to the directional solidification of the molten pool towards the BMs [29]. Additionally, the IQ map shows a lighter grey-scale level in the FZ compared to the other zones, indicating a lower density of dislocations [30]. It is important to note that the BMs exhibit heavily deformed grains, as shown in Fig. 3. During laser welding, heat transfers unidirectionally from the weld-molten pool to the BMs, resulting in static recrystallization (SRX) in the HAZ regions of both Al-TRIP and Si-TRIP sides. This SRX process promotes the formation of ultrafine-grains in the HAZs, as highlighted by the yellow dashed lines. The corresponding misorientation boundaries map in Fig. 4(b) demonstrates a high density of low-angle grain

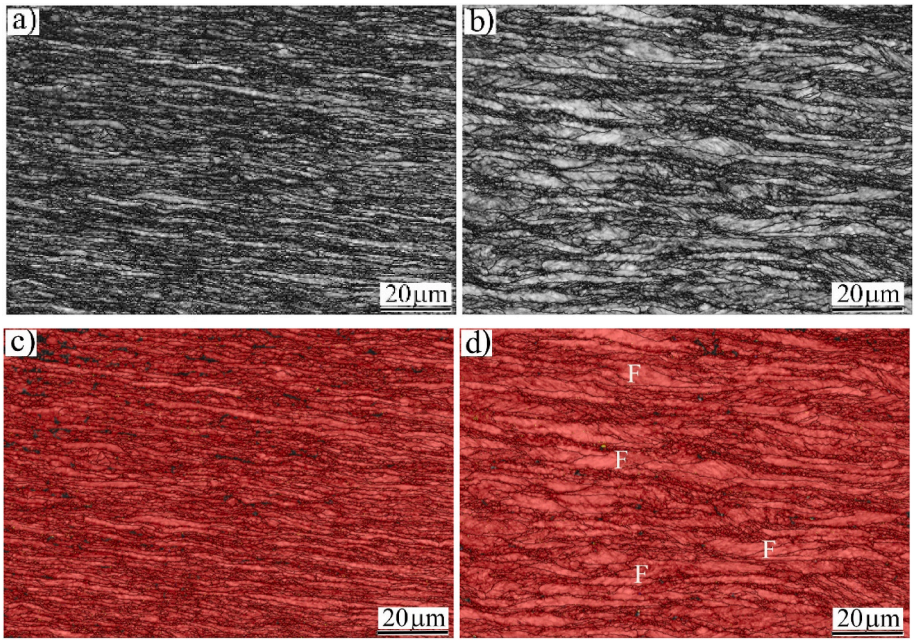

Fig. 3. EBSD maps of the microstructures of the BMs: (a) and (c) IQ map and the corresponding phase map of Al-TRIP, respectively, and (b) and (d) IQ map and the corresponding phase map of Si-TRIP, respectively. (ferrite α-bcc and martensite α′-bct indexed in red). (For interpretation of the references to color in this figure legend, the reader is referred to the Web version of this article.)

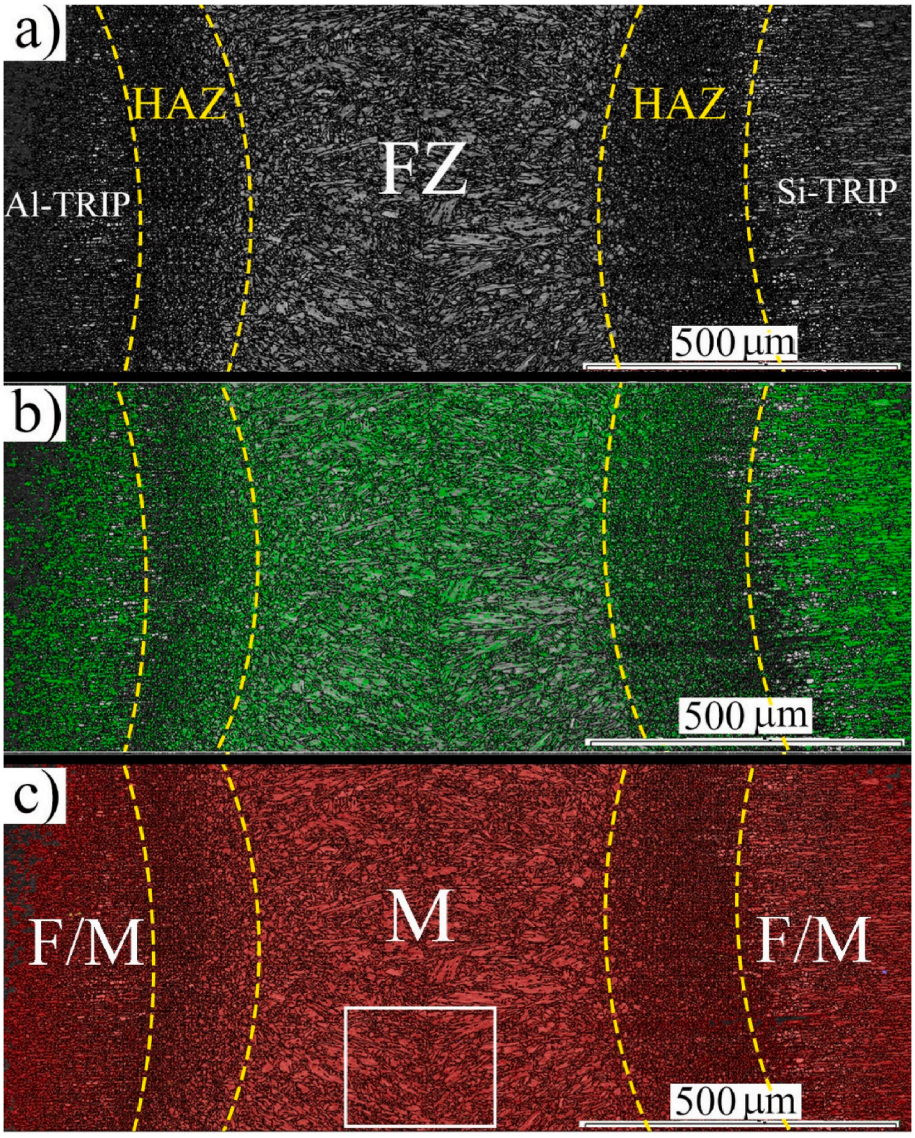

Fig. 4. EBSD analysis of the microstructure across the weld section of the laser-welded butt TRIP joint at an energy input of 24 J/mm^3: (a) IQ map depicting grain structure morphology, (b) Grain-boundary misorientation map illustrating the distribution of low-angle grain boundaries (LAGBs in green), and (c) Phase map indicating the phase structure (ferrite α-bcc (F) and martensite α′-bct (M) indexed in red). (For interpretation of the references to color in this figure legend, the reader is referred to the Web version of this article.)

boundaries (LAGBs) (<15°) in green color, present in both the FZ and the BMs. These LAGBs are known to form during the martensite transformation, occurring across lath boundaries within the martensite packets and between the sub-blocks [28,31]. In the phase map shown in Fig. 4(c), a single red-colored domain is observed for the FZ, HAZ, and BMs. Although lath martensite and ferrite phases possess different crystal structures (α′-bct and α-bcc, respectively), EBSD mapping indexes both phases as bcc-cubic crystals. However, a distinct morphological difference between martensite and ferrite is evident in Fig. 4(c). Furthermore, the high density of LAGBs in the FZ suggests the presence of lath martensite without the formation of retained austenite. This finding aligns with the study conducted by Kong et al. [32], where they reported a fully martensitic microstructure with a significant density of LAGBs in the weld zone during laser welding between boron steel and TRIP steel. Overall, the microstructure analysis of the laser-welded TRIP steels by EBSD provides valuable insights into the grain structure morphology, the presence of dislocations, the occurrence of SRX in the HAZs, and the formation of LAGBs.

Fig. 5 displays an enlarged view of the microstructure within the highlighted region of Fig. 4(c) by the white rectangular, providing a detailed illustration of the microstructural characteristics observed within the FZ during the laser welding of TRIP steels. The Image Quality (IQ) map in Fig. 5(a) reveals the presence of a lath martensite structure within the FZ. This non-equilibrium phase arises from the thermal transformation of austenite to martensite, facilitated by the high temperature in the FZ reaching approximately 2000 °C, exceeding the melting points of the steels. The rapid solidification due to a fast cooling rate of approximately 100 °C/s further enhances the formation of the lath martensite phase [33]. A notable feature of the martensitic grain structure in laser-welded TRIP steels is the presence of columnar grains derived from the prior austenite grains (PAGs), as depicted in Fig. 5(b). The unidirectional heat flux towards the BMs during laser welding results in the elongated columnar morphology of the PAGs primarily directed towards the BMs [34,35]. To estimate the PAG size, the equivalent circle diameter method was employed [29,34], and different size ranges of PAGs are represented by specific colors. In the map, PAGs within the yellow color range, measuring between 30.7 and 41 µm, constitute approximately 27.3% of the total grains. The average size of the lath martensite PAGs in the FZ of Al-TRIP and Si-TRIP at an Energy Input (EI) of 24 J/mm^3 is approximately 30 µm. It is well established that the lath martensite structure exhibits a density of dislocations and low-angle grain boundaries (LAGBs) with angles less than 15°, characteristic of the fine components [36]. The martensitic structure within the FZ, as shown in Fig. 5(a), displays a moderate density of LAGBs (~30%), represented by the green color. Fig. 5(c) presents the crystallographic orientations of the martensite components, depicted through the

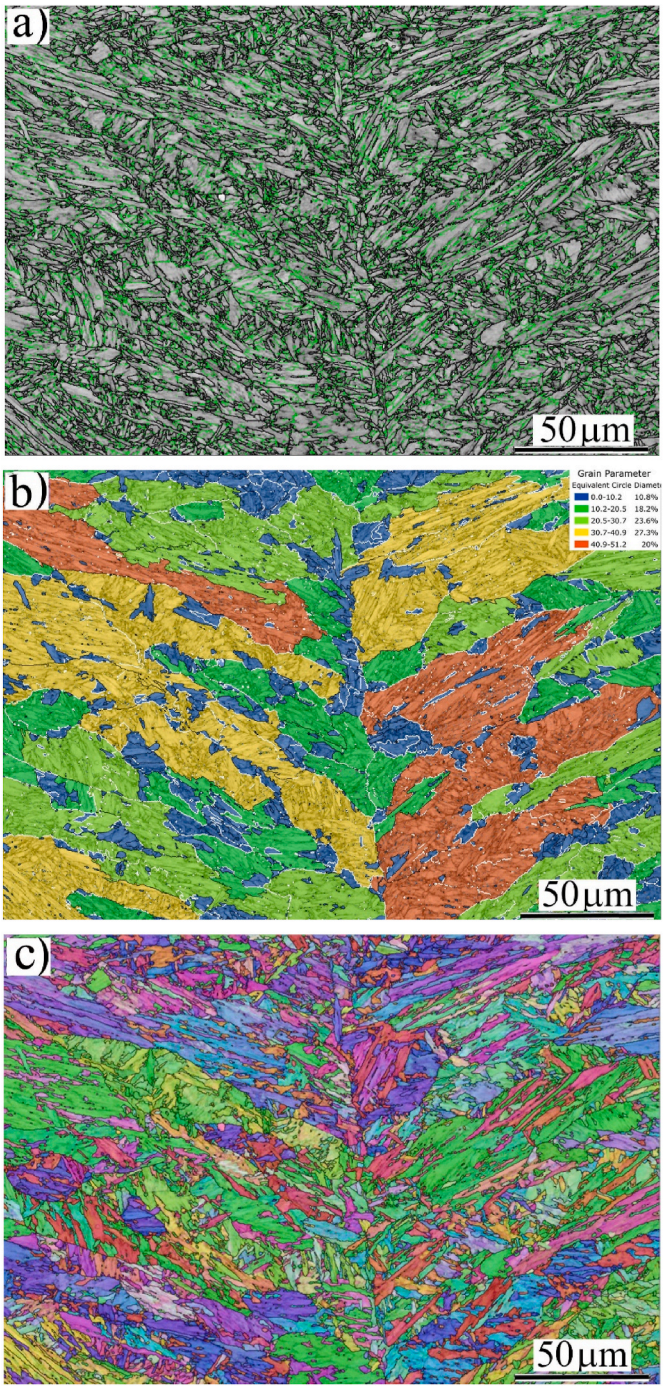

Fig. 5. Microstructural characteristics of the weld zone in the Al-TRIP/Si-TRIP joint revealing the typical lath martensite structure: (a) EBSD-IQ map combined with the Misorientation map (green color representing LAGBs of 2–15°), (b) Distribution of grain sizes in the prior austenite grains, and (c) EBSD-IPF map. (For interpretation of the references to color in this figure legend, the reader is referred to the Web version of this article.)

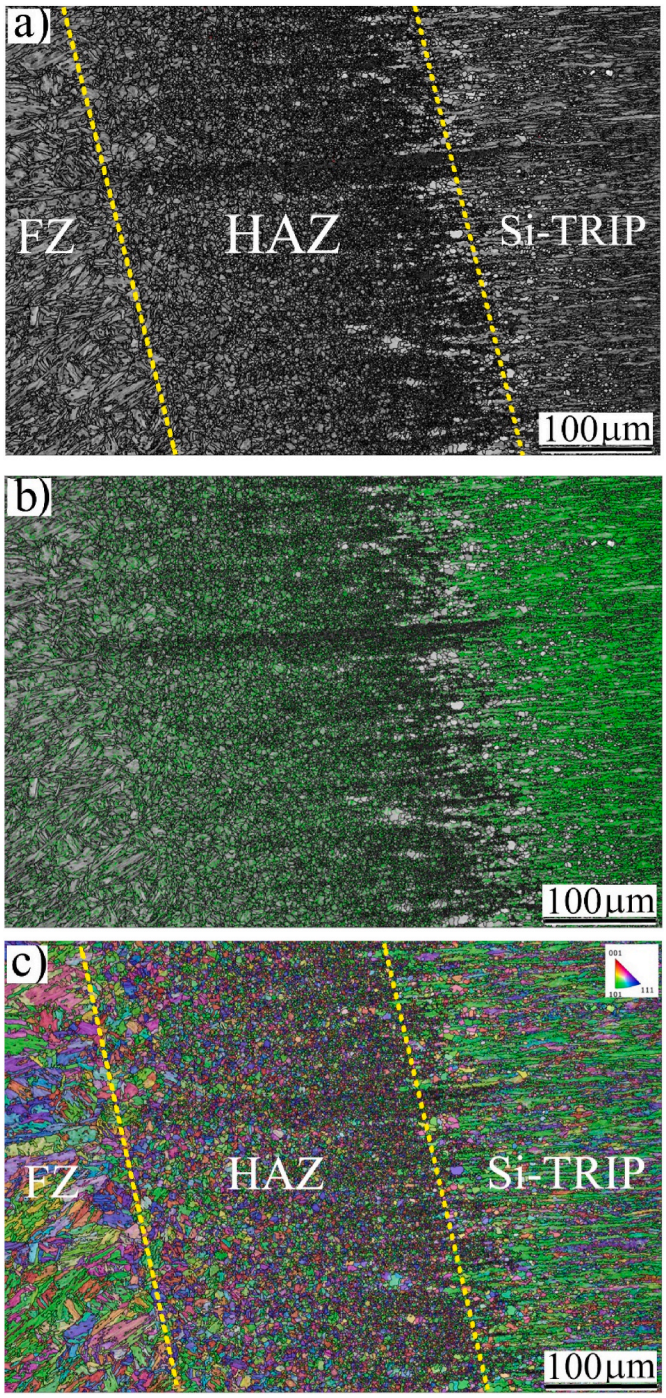

Fig. 6. Microstructure characterization of the HAZ adjacent to the Si-TRIP BM: (a) EBSD- IQ map showing the HAZ boundaries outlined by yellow dashed lines, (b) EBSD misorientation map highlighting low-angle boundaries (2–15°) in green, and (c) EBSD-IPF map. (For interpretation of the references to color in this figure legend, the reader is referred to the Web version of this article.)

corresponding orientation map (inverse pole figure, IPF). It is observed that the columnar grains predominantly exhibit texture in ⟨111⟩ orientation (blue color) and ⟨101⟩ orientation (green color).

Fig. 6 illustrates the microstructure of the HAZ located on the Si-TRIP side of the BMs. A notable characteristic of the HAZ's grain structure is the presence of an ultrafine-grained structure, as depicted in Fig. 6(a). This grain refinement in the HAZ can be attributed to rapid recrystallization. Previous studies have reported that the recrystallization of martensite occurs within the temperature range of 600–700 °C [37]. The corresponding misorientation boundary map is presented in Fig. 6(b). It is evident that the misorientations in the adjacent regions of the HAZ exhibit significant variations. Due to the heavy cold deformation experienced by the BM, a substantial density of Low-Angle Grain Boundaries (LAGBs) amounting to 58% is observed. However, the density of misorientations along the recrystallized grains in the HAZ is comparatively lower than that in the BM. Fig. 6(c) displays the orientation map of the different grain structures within the adjacent zones. The fine-equiaxed

grains in the HAZ exhibit a ⟨111⟩ crystallographic orientation, depicted in blue color. On the other hand, the elongated-pancaked grains in the BM predominantly display a ⟨101⟩ crystallographic orientation.

The fine microstructure characteristics of the HAZ near the BM Si-TRIP in laser-welded TRIP joint are depicted at high magnification in Fig. 7, revealing important details. Fig. 7(a) displays equiaxed recrystallized fine-grains of martensite and ferrite in the HAZ. Notably, the grain structure of the HAZ exhibits a low density of low-angle grain boundaries (LAGBs), approximately 20%, indicating the occurrence of recovery and dislocation substructure annihilation during the rapid recrystallization process.

Fig. 7(b) provides a closer look at the grains within the rectangular region highlighted in Fig. 7(a). Detailed observations reveal distinct characteristics of the ferrite grains "F" compared to the martensite grains "M". The ferrite grains exhibit a different grey level and morphology, while the martensite grains display a darker grey color, finer structure, and lath-like morphology within the region marked by the dashed yellow lines. The rapid recrystallization mechanism in the martensite is facilitated by the high density of dislocations present in the lath martensite structure [38]. The corresponding EBSD-phase map, shown in Fig. 7(c), illustrates the presence of a small fraction of austenite (approximately 2%) in the HAZ, represented by the blue color. The austenite grains are of microscale size and primarily located at the boundaries of the fine martensitic grains. Previous research by Amirthalingam et al. [39] investigated the phase fields and transformation temperatures of Si-TRIP steel using a pseudo binary phase diagram within a carbon content range of 0–1 wt%. At a carbon content of 0.25% in Si-TRIP, the austenite transformation temperature (Ac3) is approximately 850 °C. Considering that the temperature in the molten weld pool, i.e., FZ, during laser welding can reach peaks of 2000 °C, the temperature in the HAZ can reasonably reach around 1000 °C due to heat transfer [40]. As a result, the HAZ undergoes reversion-austenitic transformation through fast heating and subsequent martensitic transformation during rapid cooling. This is supported by the presence of retained austenite (approximately 2%) in the HAZ microstructure, as shown in Fig. 7(c). The fast austenitic transformation of the deformed martensite and ferrite grains during rapid heating of the HAZ can be attributed to the high energy stored within the deformed structure and the presence of defects, which provide nucleation sites and promote fast diffusion [41–43]. It is well established that the ferrite-to-austenite transition is a diffusion-controlled transformation [44,45]. Therefore, it is reasonable to assume that the ferrite grains "F" observed in the HAZ microstructure (Fig. 7(b)) result from insufficient available time to fully complete the transformation from ferrite to austenite due to the rapid heating process.

The grain size distribution of the newly recrystallized grains in the HAZ is presented in Fig. 7(d). The distribution reveals the presence of predominantly ultrafine grains, with diameters primarily less than 1 μm. Additionally, a small fraction, approximately 10%, of the grains exhibit sizes larger than 2 μm. These observations indicate that the deformed ferrite grains have undergone rapid recrystallization and growth, attributed to the fast recrystallization kinetics of ferrite [46]. Consequently, the HAZ exhibits a fine grain structure, with relatively small ferrite grains on the order of 3 μm, as illustrated in Fig. 7(b).

Similarly, a fine grain structure is observed in the HAZ of Al-TRIP, as indicated by the dashed yellow lines in Fig. 8(a). Furthermore, a comparison between Fig. 6(a) and 7(a) reveals a wider HAZ in Si-TRIP compared to Al-TRIP, suggesting a higher heat flux in the former. A quantitative estimation of the HAZ sizes, based on direct comparison, indicates that the HAZ size in Si-TRIP is approximately 250 μm, whereas in Al-TRIP it is around 160 μm. This difference can be attributed to the offset of the laser beam by 0.15 mm towards the thicker BM Si-TRIP, as stated in the welding setup (see Section 2.1). Fig. 8(b) provides a magnified view of the HAZ microstructure in the BM Al-TRIP. It reveals the presence of ultrafine grains of lath martensite and ferrite, with a moderate fraction of low-angle grain boundaries (LAGBs) highlighted in

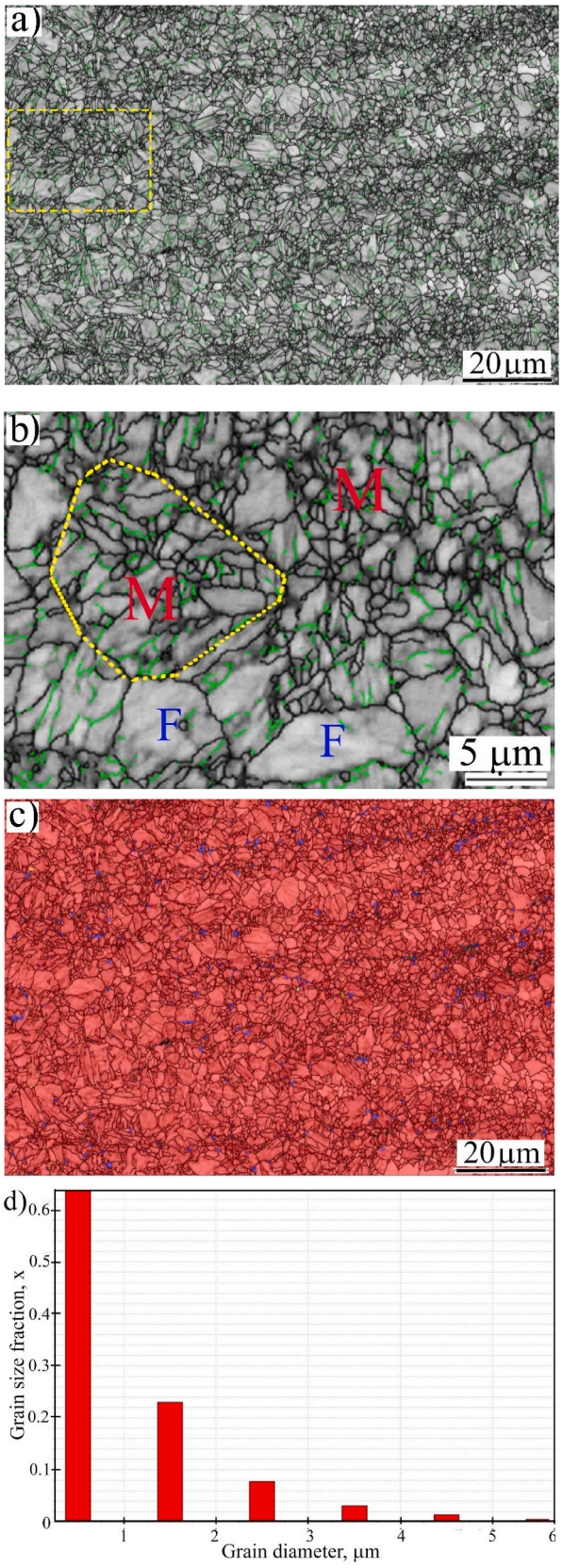

Fig. 7. Microstructural characterization of the HAZ near the BM Si-TRIP at high magnification: (a) EBSD-IQ map, (b) Enlarged view of the marked zone in (a), (c) EBSD-phase map, and (d) Grain size distribution analysis of the microstructure in (a). (ferrite α-bcc and martensite α′-bct indexed in red, austenite γ-fcc indexed in blue)). (For interpretation of the references to color in this figure legend, the reader is referred to the Web version of this article.)

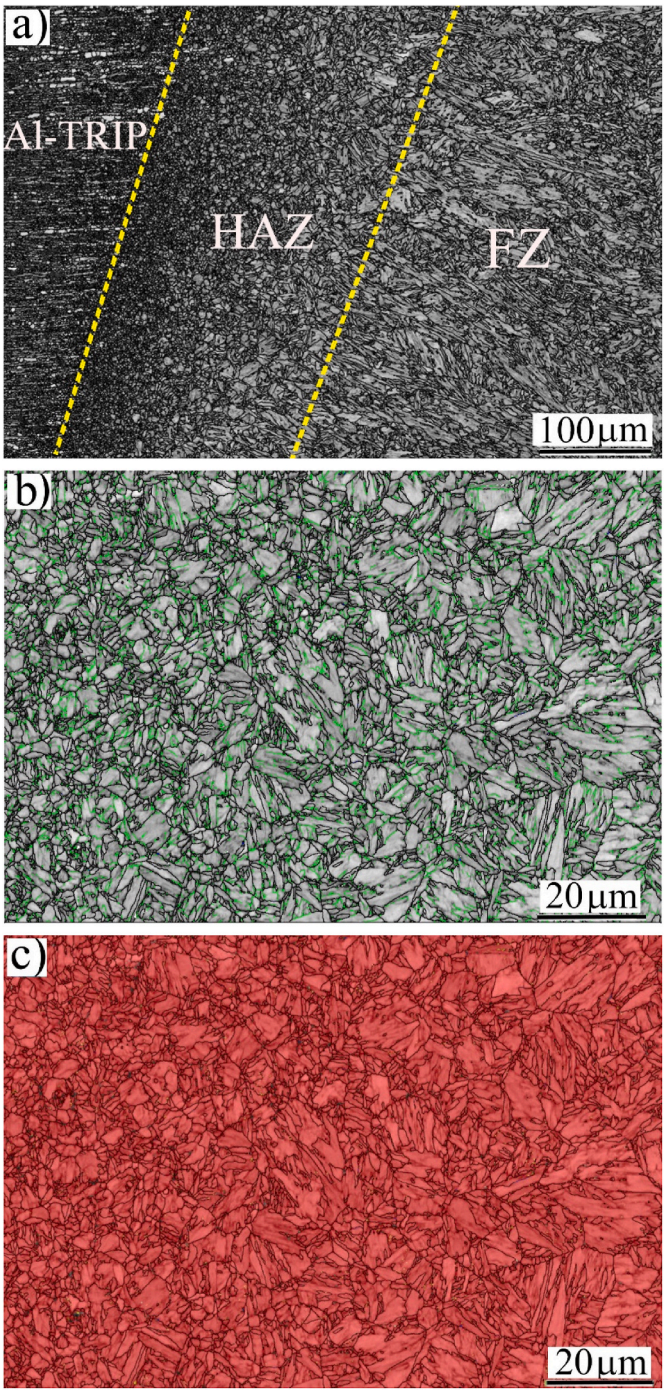

Fig. 8. EBSD maps of the HAZ of the BM Al-TRIP: (a) general view, IQ map at low magnification, (b) IQ map at high magnification, and (c) phase map of (b). (ferrite α-bcc and martensite α′-bct indexed in red). (For interpretation of the references to color in this figure legend, the reader is referred to the Web version of this article.)

green color. Furthermore, the corresponding phase map in Fig. 8(c) indicates the absence of retained austenite in the HAZ microstructure. Previous work by Amirthalingam et al. [39] illustrated the phase fields and transformation temperatures of Al-TRIP steel through a pseudo binary phase diagram. At the carbon content of 0.25% C, corresponding to the composition of Al-TRIP, the austenite transformation temperature (Ac3) is approximately 1000 °C. Thus, it is reasonable to expect that the HAZ in Al-TRIP does not undergo austenitic transformation during fast heating, as confirmed by the phase map in Fig. 8(c), which does not reveal any retained austenite, unlike the HAZ in Si-TRIP (see Fig. 7(c)). Overall, the microstructure analysis of the HAZs in laser-welded TRIP steels joint provides valuable insights into the complex interplay of recrystallization, phase transformations, and the influence of fast heating during the welding process.

3.2. TEM microstructure analysis

Fig. 9(a) presents a bright-field (BF) STEM image of the entire lamella extracted from the HAZ of Si-TRIP. The BF micrograph reveals the presence of fine polygonal ferrites (α-bcc) alongside a refined martensite lath structure. To investigate the specific regions of interest, high-magnification micrographs of the selected regions in Fig. 9(a) are shown in Fig. 9(b) and (d).

Adjacent to the ferrite grain boundaries, the presence of martensite/austenite (M/A) islands can be observed. To further analyze these regions, dark-field (DF) imaging techniques were employed. Fig. 9(c) displays the corresponding DF image, recorded using the (200) diffraction spot from the selected area diffraction pattern based on the $[110]_{RA}$ zone axis. This DF image provides insights into the distribution of certain features, such as the M/A islands.

In Fig. 9(e), a magnified view of a specific region, marked with green borders in Fig. 9(a), reveals the presence of numerous interwoven films of η-Fe_2C precipitates. These precipitates are nanoscale size carbides plate-like particles, and their existence is further confirmed by the corresponding DF image in Fig. 9(e). The inset of Fig. 9(f) presents the selected area diffraction (SAD) pattern associated with this region, providing additional confirmation of the presence of Fe_2C precipitates.

According to the research conducted by Lu et al. [47], these nanoscale plate-like η-Fe_2C carbides exhibit specific dimensions, with a width of 1.52 ± 0.62 nm and a facet length of 3.1 ± 0.4 nm. The orientation relationship with the matrix $[(113)_{ferrite}//(121)_{Fe2C}]$ further supports the identification of these precipitates as Fe_2C [48,49]. The TEM analysis provides valuable insights into the microstructural characteristics and the presence of nanoscale η-Fe_2C precipitates within the HAZ of Si-TRIP.

The TEM analysis of the HAZ of the BM Al-TRIP, Fig. 10, reveals certain similarities and differences when compared to the TEM analysis of the HAZ of the BM Si-TRIP HAZ, see Fig. 9. In both cases, the micrographs show a combination of polygonal ferrite grains and a fine martensite lath structure. However, the Al-TRIP HAZ zone exhibits a relatively larger polygonal ferrite grain compared to the Si-TRIP HAZ zone.

The magnified views in Fig. 10(b) and (d) of the HAZ in Al-TRIP highlight the presence of finely divided retained austenite (RA) films located at the interlath regions. This is similar to the Si-TRIP HAZ zone, where the presence of a certain fraction of martensite/austenite (M/A) islands adjacent to the ferrite grain boundaries was identified.

DF imaging was utilized in both cases to provide further information. The DF image in Fig. 10(c) of the HAZ in Al-TRIP, recorded using the (200) diffraction spot, reveals the distribution of the RA films. Similarly, the DF image in Fig. 9(c) of the HAZ in Si-TRIP shows the presence of fine Fe_2C precipitates.

Fig. 10(b,e) of the HAZ in Al-TRIP depict the presence of nanosized Fe_2C precipitates within the ferrite laths, similar to Fig. 9(b,d) of the HAZ in Si-TRIP. The corresponding dark-field images, presented in Fig. 10(f) for Al-TRIP and Fig. 9(f) for Si-TRIP, provide additional visualization of these precipitates.

The orientation relationship between the Fe_2C precipitates and the ferrite matrix is consistent in both cases. In the HAZ in Si-TRIP, the precipitates were identified as Fe_2C with an orientation relationship $[(113)_{ferrite}//(121)_{Fe2C}]$. Similarly, in the HAZ in Al-TRIP, the orientation relationship was $[(001)_{ferrite}//(001)_{Fe2C}]$ [50,51]. The TEM analyses of both the HAZs in Si-TRIP and Al-TRIP reveal the presence of finely divided Fe_2C precipitates and the distribution of retained austenite or martensite/austenite islands. These microstructural

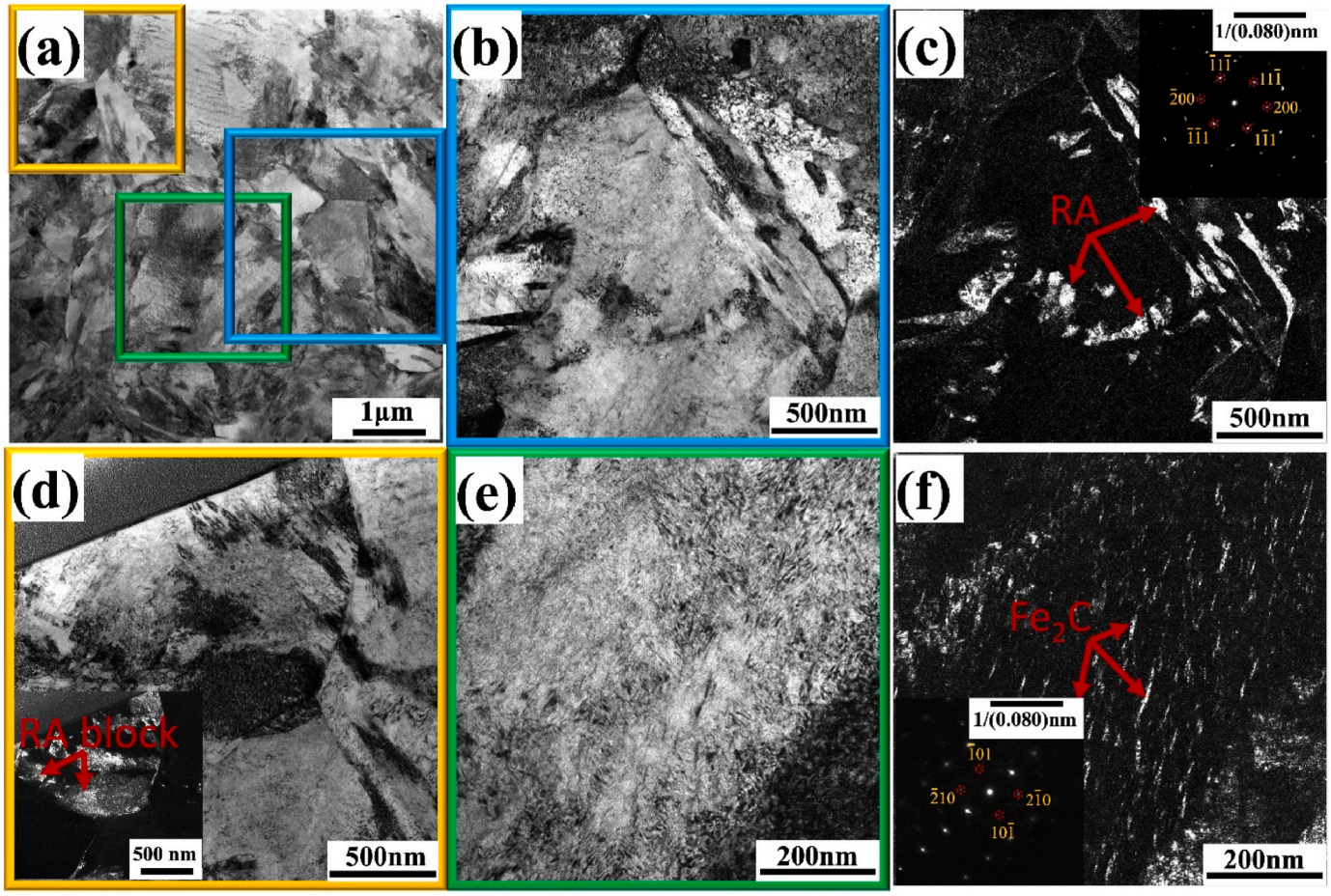

Fig. 9. Microstructural characteristics of the HAZ in Si-TRIP by TEM analysis: (a) Bright-field STEM micrograph, (b,d, and e) magnified views of specific regions in (a). Additionally, corresponding dark-field images are shown, highlighting the presence of retained austenite (c) and nano carbides η-Fe_2C (f).

features contribute to the understanding of the strengthening mechanisms and mechanical properties in the respective HAZs.

In general, transition carbides (Fe_2C) exhibit a certain level of coherence with the ferrite/martensite matrix, thereby contributing to strengthening through coherency mechanisms. This coherence between Fe_2C and the matrix enhances hardness and improves the rate of work hardening [49,51].

3.3. Mechanical performance of the TRIP joint

The tensile properties of laser-welded Al-TRIP/Si-TRIP joints and their corresponding BMs are presented in Fig. 11. During tensile testing, the applied force leads to stress and strain, which are influenced by the geometrical size effect, specifically the sheet thickness [52]. In this study, the BMs had different thicknesses, with Al-TRIP at 0.9 mm and Si-TRIP at 1.3 mm. Due to the smaller cross-sectional area, the thinner Al-TRIP sheet experiences a higher stress distribution during tensile loading, leading to strain localization primarily in the cross-section of the thinner material. As a result, the tensile properties of the Al-TRIP/Si-TRIP joint closely resemble those of the BM Al-TRIP. The shape and behaviour of the tensile flow curve for the joint align with those of the BM Al-TRIP, as shown in Fig. 11. It is important to note that the presence of hard structures, such as the FZ and HAZ, in the weld zones supports the overall plastic deformation of the thinner Al-TRIP and contributes to subsequent plasticity failure.

Table 2 provides an overview of the mechanical properties of the Al-TRIP/Si-TRIP joint and the BMs. It is evident that the BM Al-TRIP exhibits higher mechanical strengths compared to Si-TRIP. For instance, the yield strength (YS) and tensile strength (TS) of Al-TRIP are measured at 1100 MPa and 1150 MPa, respectively, while Si-TRIP demonstrates values of 1035 MPa and 1110 MPa. This difference can be attributed to the solute-strengthening effect of both Al and Si in TRIP steels. However, Al provides a lesser solid solution-strengthening effect compared to Si [53]. With a higher Al content (2.4 wt %) in Al-TRIP and a lower Si content (1.5 wt %) in Si-TRIP, the solid solution strengthening effect is more pronounced in Al-TRIP. Furthermore, the plastic deformation capacity of the Al-TRIP/Si-TRIP joint is noticeably limited under tensile deformation, exhibiting an elongation of approximately 2.5%. This limitation is attributed to the severe work-hardened structure of the BM Al-TRIP, which ultimately leads to joint fracture. Hence, the tensile properties and mechanical strengths of the Al-TRIP/Si-TRIP joint closely resemble those of the corresponding BM Al-TRIP. The presence of hard structures in the weld zones supports overall deformation behaviour, while the differing solute-strengthening effects of Al and Si influence the mechanical properties. Understanding these relationships provides valuable insights into the performance and limitations of laser-welded TRIP joints in practical applications.

The H_{IT} measurements provide valuable information about the mechanical properties and local hardness variations within the different zones of the laser-welded TRIP joint. Fig. 12(a) shows the load-penetration depth (P-PD) curves obtained from microindentation tests conducted on the FZ, HAZs, and BMs.

The FZ, indicated by the red solid line, exhibited high resistance to indentation with a low penetration depth of approximately 3.6 μm. This indicates a high hardness in the FZ, which can be attributed to the formation of a hard martensitic matrix during the rapid solidification

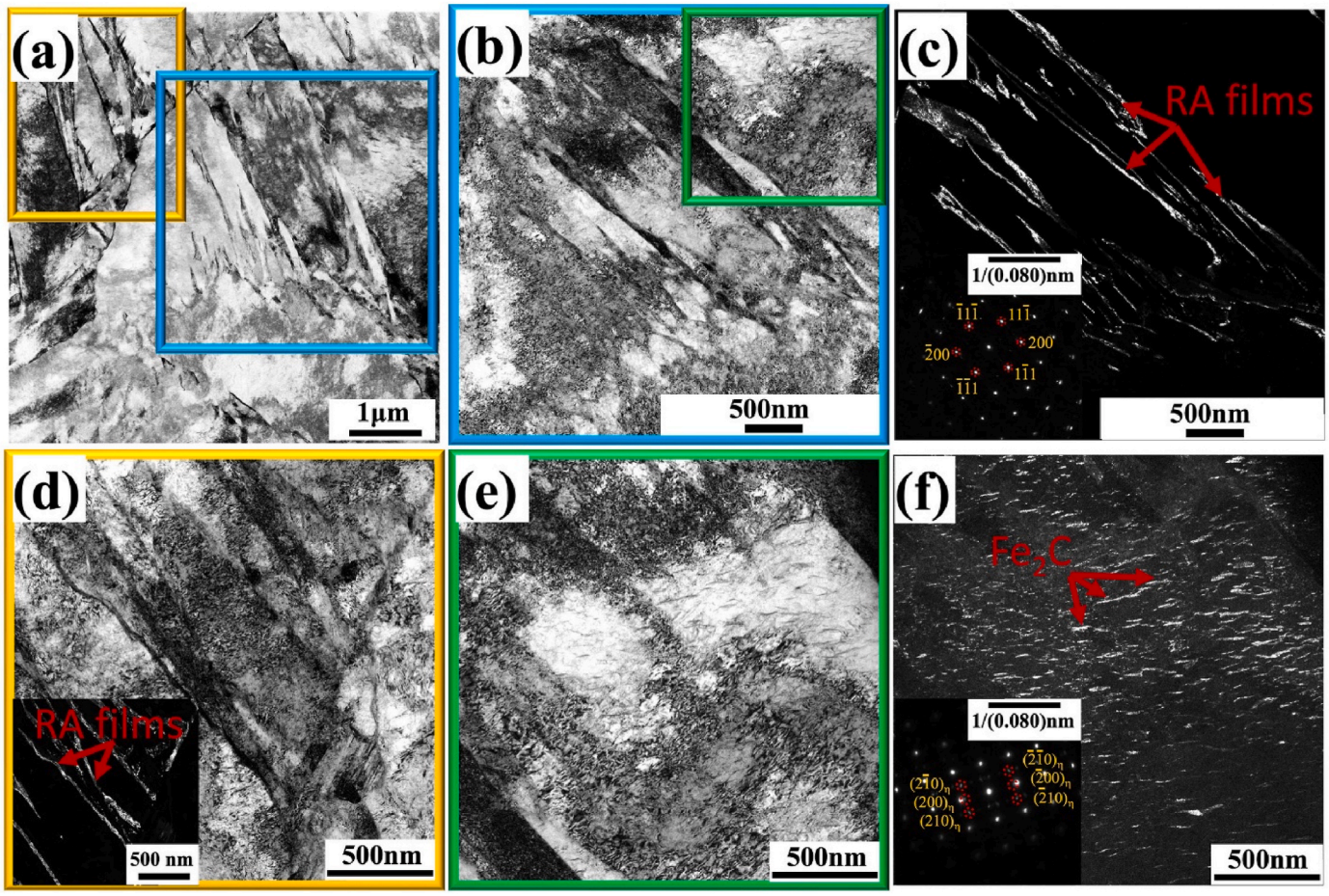

Fig. 10. Microstructural characteristics of HAZ in BM Al-TRIP through TEM analysis, (a) bright-field STEM micrograph, (b,d, and e) magnified views of specific regions, (c, and f) Corresponding dark-field images are provided, highlighting the presence of retained austenite (c) and nano carbides η-Fe_2C (f).

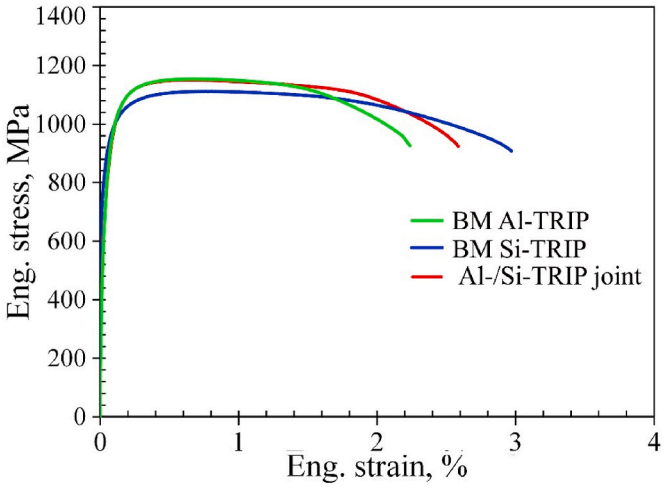

Fig. 11. Tensile flow curves of the laser-welded TRIP joint compared to the corresponding flow curves of the BMs.

process. The HAZ on the Al-TRIP side, represented by the red dashed line, displayed a slightly lower penetration depth of 3.4 μm, indicating a slightly higher hardness compared to the FZ. This can be attributed to the presence of an ultrafine-grained martensitic structure resulting from recrystallization in the heavily cold-deformed microstructure of the HAZ. On the other hand, the BMs exhibited higher penetration depths of 4 μm for Al-TRIP and 4.4 μm for Si-TRIP, indicating lower hardness values compared to the FZ and HAZs.

Table 2
Mechanical properties of the Al-/Si-TRIP joint and the BMs.

Steel code	YS, MPa	TS, MPa	El., %
BM Al-TRIP	1100	1150	2.2
BM Si-TRIP	1035	1110	3
Al-/Si-TRIP	1107	1155	2.4

In Fig. 12(b), the H_{IT} measurements and corresponding PD values are presented in the form of bar plots, providing a clear comparison of the hardness among the different zones. The FZ, represented by the shaded bar in light blue, showed a slightly lower H_{IT} compared to the HAZs located on the BMs' sides. This suggests that the FZ has a slightly lower hardness than the HAZs. The H_{IT} values for the FZ, Al-TRIP HAZ, and Si-TRIP HAZ were measured at 6.3 GPa, 6.8 GPa, and 6.6 GPa, respectively. The higher H_{IT} values observed in the HAZs can be attributed to existence of the hard M/A islands and ferrite grain refinement achieved through recrystallization. Additionally, the presence of nanosized η-Fe_2C carbides substantially enhances the precipitation strengthening mechanism within the HAZ, effectively impeding dislocation movement and resulting in enhanced mechanical properties such as hardness and yield strength [54,55]. In contrast, the BMs (Al-TRIP and Si-TRIP) exhibited significantly lower H_{IT} values of 4.6 GPa and 4.3 GPa, respectively. This is mainly due to the presence of a softer ferritic phase in the BMs' matrix, which results in a decrease in hardness.

It is important to note that the hardness measurements obtained by H_{IT} correlate with the microstructural features observed in the

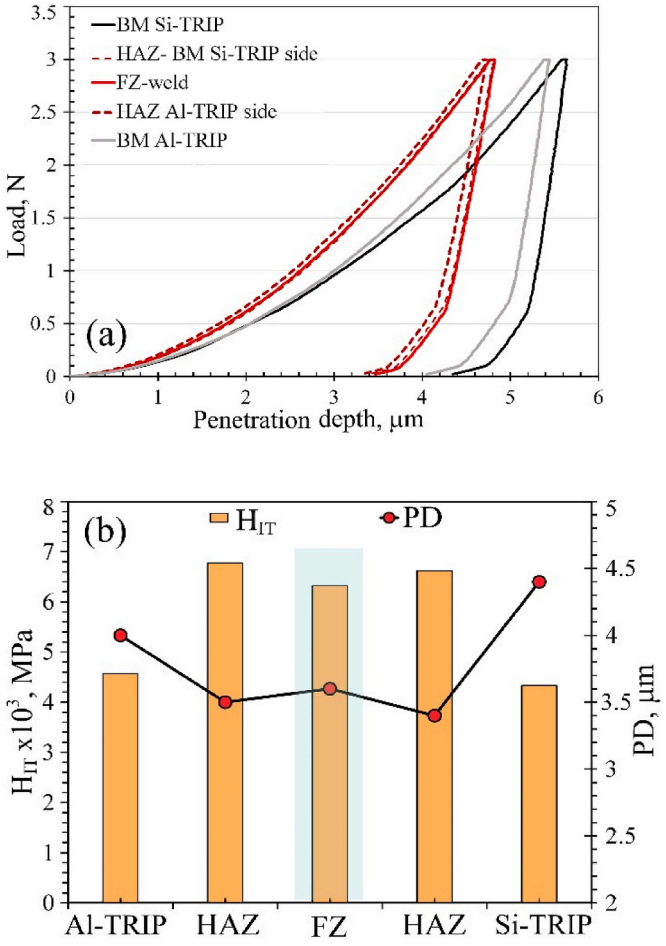

Fig. 12. Microindentation hardness (H_{IT}) measurements: (a) Load–penetration depth (P-PD) curves, and (b) H_{IT} values (bar plot) and corresponding penetration depth (DP) (line plot) of the different zones in the Al-/Si-TRIP joint, obtained from the P-PD plots in (a).

corresponding zones. The hard martensitic matrix in the FZ contributes to its higher hardness, while the ultrafine-grained martensitic structure in the HAZs enhances their hardness compared to the FZ. The lower hardness values in the BMs can be attributed to the presence of a softer ferritic phase. These hardness variations within the weldment can influence the overall mechanical properties and performance of the laser-welded TRIP joint.

The results indicate that the hardness distribution in the weldment is not uniform, and the different zones exhibit distinct hardness characteristics. This information is crucial for understanding the local mechanical behaviour and potential failure mechanisms within the joint. The observed differences in hardness can be attributed to variations in microstructural features, such as phase composition, grain size, and the presence of different phases (martensite, ferrite). These variations can significantly influence the joint's mechanical properties, including strength, toughness, and deformation behaviour.

3.4. Finite element analysis (FEA)

The aim of FEA in the present work is to simulate and analyze the mechanical behavior and deformation response of the laser-joined Al-TRIP and Si-TRIP steels. FEA enables us to study the complex interactions between the joint geometry, material properties, and applied loading conditions. By conducting FEA, we can gain insights into the stress distribution, deformation mechanisms, and performance of the joints under various loading scenarios. The ultimate goal is to better understand the structural response and optimize the design of laser-welded TRIP joints in terms of strength and integrity.

FEA provides valuable predictions of stress, strain, and deformation within the joints. It helps us assess the joint's structural integrity, identify potential failure modes, and optimize the welding parameters to enhance the joint's performance. The insights gained from FEA can guide the development and improvement of laser-welded TRIP joints in terms of strength, durability, and reliability.

The strain localization observed in the laser-welded TRIP joint plays a significant role in understanding the joint's mechanical behaviour and its potential failure mechanisms. Contours of von-mises strain on the front view of the tensile specimen after 50% elongation and at failure strain are shown in Fig. 13. The strain localization in the base region of the Al-TRIP side, along a 45° angle with respect to the tensile axis, indicates a region of concentrated deformation. The magnified view of Von-Mises strain contour in the middle of the specimen (Fig. 14(a)) shows that the FZ and HAZ experienced a much lower strain and remained mostly in the elastic region. This is in good agreement with the failure observed in the experimental specimen (sec. 3.2). This localized plastic deformation can lead to strain accumulation and potential stress concentration, which may affect the joint's overall strength, ductility, and fracture resistance. The strain localization pattern aligns with the observed failure in the experimental specimen, reinforcing the relevance of these findings. In dissimilar welded joints, strain localization is often associated with differences in strain hardening capability and microstructural inhomogeneities [56,57]. However, in this study, the hardening rates of the two alloys were found to be similar (Fig. 11). Consequently, the observed strain localization cannot be solely attributed to dissimilar strain hardening behaviours or microstructural differences between the Al-TRIP and Si-TRIP materials.

Instead, the difference in thickness between the two steels emerges as a plausible explanation for the observed strain localization. The dissimilarity in thickness leads to uneven stress distribution, resulting in localized strain concentrations in the thinner Al-TRIP side. This phenomenon indicates the influence of geometry on the mechanical response of the joint and emphasizes the importance of considering thickness variations in dissimilar welded joints.

The FEM approach employed in this study provides further insight into the deformation behaviour and stress distribution within the joint. By accurately capturing the complex interactions between geometry, material properties, and loading conditions, FE analysis offers a powerful tool for investigating strain localization and optimizing joint design. Understanding and mitigating strain localization is crucial for ensuring the structural integrity and mechanical performance of laser-welded TRIP joints. Future research could focus on exploring strategies to minimize strain concentrations, such as optimizing joint design, adjusting welding parameters, or introducing interlayers with tailored mechanical properties. Additionally, investigating the effects of other factors, such as welding speed and heat input, on strain localization patterns would contribute to a more comprehensive understanding of the behaviour of laser-welded TRIP joints. These factors were not studied in the present manuscript.

Fig. 14(b) clearly demonstrates that the stress levels are higher in the thinner Al-TRIP material, as expected. This is due to the smaller cross-sectional area of the Al-TRIP specimen, which results in a higher stress distribution. Additionally, stress concentration is observed in the Al-TRIP specimen adjacent to the weld, while significantly lower stress levels are generated in the Si-TRIP side. This difference in stress distribution can be attributed to the dissimilar material properties and geometry of the joint.

To further analyze the stress distribution, the stress profile along the center line of the tensile specimen at the failure strain is presented in Fig. 15. It can be seen that the von Mises stress increases from approximately 800 MPa in the Si-TRIP specimen to around 1200 MPa in the Al-TRIP side. This stress concentration phenomenon is commonly observed in joints where there is a significant mismatch in elastic properties

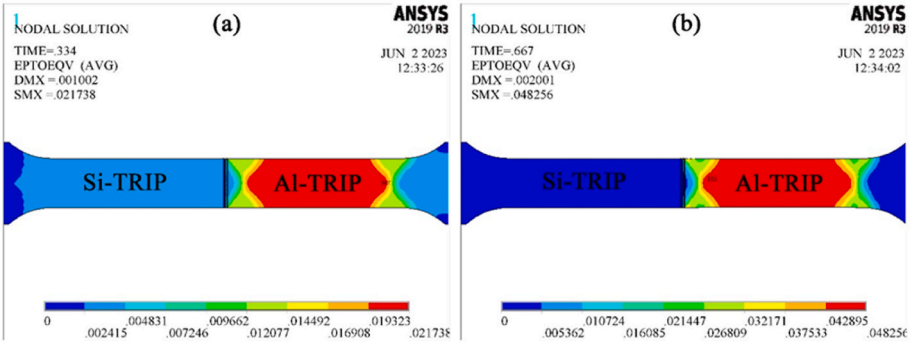

Fig. 13. Distribution of Von-Mises strain on the front face of the tensile specimen at a) 50% of the failure strain and b) failure strain.

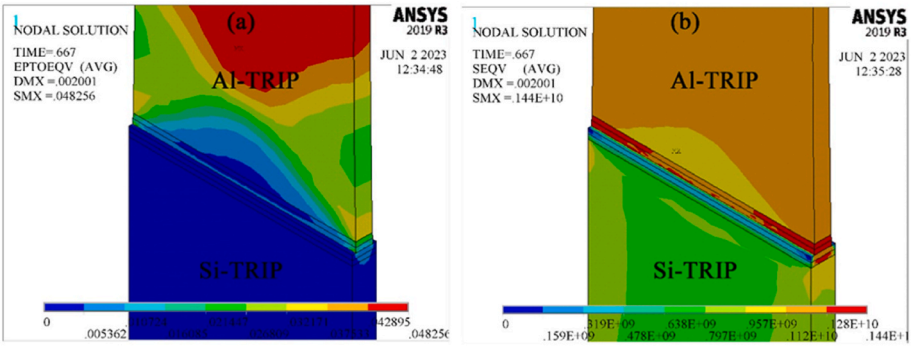

Fig. 14. Distribution of (a) Von-Mises strain contour and (b) Von-Mises stress contour at the middle region of the tensile specimen at the point of failure strain.

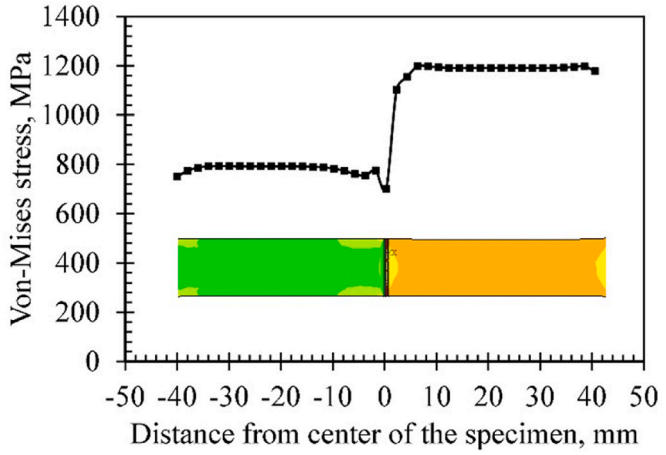

Fig. 15. Von-Mises stress distribution along the center line of the tensile specimen at the point of failure strain.

between the materials [58]. In the present work, the variation in cross-sectional area, resulting from the difference in thickness between the materials, contributes to the observed stress concentration. The abrupt increase in stress occurs specifically in the Al-TRIP specimen adjacent to the weld line.

Interestingly, despite the sharp increase in stress near the weld line, the maximum value of the von Mises strain and failure occurrence are found at a distance from the weld line, as depicted in Figs. 13 and 14. This observation suggests that factors other than stress concentration contribute to the failure of the joint. One important factor is the hardness and strength of the HAZ and FZ. The HAZ and FZ exhibit higher hardness and strength compared to the BMs, as revealed in Fig. 12(b). These hard microstructures influence the deformation behaviour of the joint, causing strain localization and potentially leading to failure at locations away from the weld line.

Additionally, the thermal softening of the BM under the welding process can also contribute to the observed behaviour [59]. Higher heat inputs in the welding process can result in localized softening of the BM, making it more susceptible to deformation and failure. This thermal softening effect, combined with the presence of harder microstructures in the HAZ and FZ, further influences the strain distribution and failure behaviour of the joint.

The stress distribution and stress concentration patterns revealed by finite element modelling provide valuable information for understanding the mechanical response and potential failure mechanisms of the laser-welded TRIP joint. These findings highlight the importance of considering material properties, geometry, and welding parameters in joint design and optimization. Mitigating stress concentration can be achieved through various strategies such as adjusting welding parameters, optimizing joint geometry, or introducing intermediate layers with tailored mechanical properties. Furthermore, investigating the effects of different heat inputs and thermal cycles on stress distribution would provide deeper insights into the behaviour of laser-welded TRIP joints and aid in improving their mechanical performance and reliability.

4. Conclusions

A comprehensive investigation was conducted on the microstructural evolution and associated strengthening mechanisms in thin laser-welded cold-rolled TRIP sheets with high Al and Si content, and a comparison was made with the behaviour of the BMs, Al-TRIP and Si-TRIP. The following key conclusions were drawn from the study:

1. Microstructural analysis using EBSD mapping revealed that the FZ exhibited a fully transformed lath martensitic structure with elongated columnar prior austenite grains, averaging 30 μm in size.
2. Ultrafine-grained structures, with diameters of 1 μm and 1.3 μm, were unexpectedly observed in the HAZs of Si-TRIP and Al-TRIP,

respectively. These ultrafine-grained structures were promoted by fast heating, which activated the recrystallization mechanism of the martensitic/ferritic grains.

3. Further characterization using TEM provided detailed insights into the microstructural features and mechanisms occurring at the nanoscale level. Refined polygonal ferrites (α-bcc) together with ultrafine martensite lath structure observed at HAZ. Moreover, existence of a certain fraction of martensite/austenite (M/A) island and fine Fe_2C precipitates are identified within ferrite grains.
4. Surprisingly, the H_{IT} values of the HAZs were found to be higher than those of the FZ and the BMs Al-TRIP and Si-TRIP. For example, the H_{IT} values for the HAZs, FZ, BM Al-TRIP, and Si-TRIP were 6.8 GPa, 6.3 GPa, 4.6 GPa, and 4.3 GPa, respectively. This increase in hardness can be attributed to the grain refinement mechanism occurring in the martensitic/ferritic grains within the HAZs together with existence of the hard M/A islands. Additionally, formation of η-Fe_2C carbides provides extra strengthening by coherency mechanisms and enhance the hardness.
5. The tensile properties of the Al-/Si-TRIP joint were found to be comparable to those of the BM Al-TRIP. This similarity can be attributed to the higher strength observed in the weld zones, specifically the FZ and HAZs, in comparison to BMs. As a result, the tensile failure of the joint transpired in the thinner BM, Al-TRIP steel.
6. Finite element analysis of the dissimilar joint under tensile testing revealed that the thinner Al-TRIP side experienced significantly higher strain compared to the Si-TRIP side. Despite the stress concentration observed at the interface of the two steels, the strain localized in the base region where the FZ and HAZs were not extensively involved. This behaviour can be attributed to the higher strength exhibited by the latter two regions.

These findings contribute to a better understanding of the microstructural characteristics, mechanical properties, and failure mechanisms in laser-welded TRIP joints. Hence, the results have implications for the design and optimization of such joints, considering the role of different regions, grain refinement mechanisms, and stress distribution.

CRediT authorship contribution statement

Atef Hamada: Visualization, Formal analysis, Conceptualization, Writing - original draft, Writing - review & editing. **Ali Khosravifard:** conducting finite element modelling. **Sumit Ghosh:** Methodology, Formal analysis. **Matias Jaskari:** Methodology, Formal analysis. **Marion Kreins:** Methodology. **Walaa Abd-Elaziem:** Writing – original draft. **Mohamed Wahba:** Methodology. **Essam Ahmed:** Conceptualization, Visualization. **Tarek Allam:** Methodology, Project administration.

Declaration of competing interest

The authors declare that they have no known competing financial interests or personal relationships that could have appeared to influence the work reported in this paper.

Data availability

No data was used for the research described in the article.

Acknowledgement

The authors would like to extend their sincere gratitude to ThyssenKrupp Steel Europe AG (TKSE), Germany, for generously providing the experimental Al-TRIP and Si-TRIP steel sheets. The successful completion of the experimental study, encompassing mechanical tests, SEM-EBSD experiments, and TEM examination, owes its realization to the invaluable support provided by the Business Finland-FOSSA project-Fossil-Free Steel Applications, under grant number 5498-31-2021. Their funding has been instrumental in facilitating our research and driving its significant outcomes.

References

[1] K. Kawajiri, M. Kobayashi, K. Sakamoto, Lightweight materials equal lightweight greenhouse gas emissions?: a historical analysis of greenhouse gases of vehicle material substitution, J. Clean. Prod. 253 (2020), https://doi.org/10.1016/j.jclepro.2019.119805.
[2] A. Giampieri, J. Ling-Chin, Z. Ma, A. Smallbone, A.P. Roskilly, A review of the current automotive manufacturing practice from an energy perspective, Appl. Energy 261 (2020), https://doi.org/10.1016/j.apenergy.2019.114074.
[3] J.L. Bocos, F. Zubiri, F. Garciandía, J. Peña, A. Cortiella, J.M. Berrueta, F. Zapiráin, Application of the diode laser to welding on tailored blanks, Weld. Int. 19 (2005) 539–543, https://doi.org/10.1533/wint.2005.3447.
[4] E.S. Perdahcıoğlu, H.J.M. Geijselaers, Mechanical behavior of multi-phase steels comprising retained austenite, Materials (Basel) 15 (2022), https://doi.org/10.3390/MA15020498.
[5] M. Amirthalingam, M.J.M. Hermans, L. Zhao, I.M. Richardson, Quantitative analysis of microstructural constituents in welded transformation-induced-plasticity steels, Metall. Mater. Trans. A Phys. Metall. Mater. Sci. 41 (2010) 431–439, https://doi.org/10.1007/S11661-009-0117-6/TABLES/4.
[6] B.C. De Cooman, Structure–properties relationship in TRIP steels containing carbide-free bainite, Curr. Opin. Solid State Mater. Sci. 8 (2004) 285–303, https://doi.org/10.1016/J.COSSMS.2004.10.002.
[7] D.Y. Chen, L.M. Wang, C.Z. Wang, L.K. Yuan, T.Y. Zhang, Z.Z. Zhang, Finite element based improvement of a light truck design to optimize crashworthiness, Int. J. Automot. Technol. 16 (2015) 39–49, https://doi.org/10.1007/S12239-015-0004-7/METRICS.
[8] M. Xia, Z. Tian, L. Zhao, Y.N. Zhou, Metallurgical and mechanical properties of fusion zones of TRIP steels in laser welding, ISIJ Int. 48 (2008) 483–488, https://doi.org/10.2355/ISIJINTERNATIONAL.48.483.
[9] M. Xia, Z. Tian, L. Zhao, Y.N. Zhou, Fusion zone microstructure evolution of Al-alloyed TRIP steel in diode laser welding, Mater. Trans. 49 (2008) 746–753, https://doi.org/10.2320/MATERTRANS.MRA2007271.
[10] J.J. Guzman-Aguilera, C.J. Martinez-Gonzalez, V.H. Baltazar-Hernandez, S. Basak, S.K. Panda, M.H. Razmpoosh, A. Gerlich, Y. Zhou, Influence of SC-HAZ microstructure on the mechanical behavior of Si-TRIP steel welds, Mater. Sci. Eng. A. 718 (2018) 216–227, https://doi.org/10.1016/J.MSEA.2018.01.108.
[11] T.K. Han, S.S. Park, K.H. Kim, C.Y. Kang, I.S. Woo, J.B. Lee, CO2 laser welding characteristics of 800 MPa class TRIP steel, ISIJ Int. 45 (2005) 60–65, https://doi.org/10.2355/ISIJINTERNATIONAL.45.60.
[12] B. Zhang, Y. Dong, Y. Du, R.D.K. Misra, H.Y. Wu, X.N. Wang, W.Z. Zhao, L.X. Du, Microstructure and formability performance of fiber laser welded 1.2 GPa grade hot-rolled TRIP steel joints, Opt Laser. Technol. 143 (2021), https://doi.org/10.1016/J.OPTLASTEC.2021.107341.
[13] T. Wang, M. Zhang, R. dong Liu, L. Zhang, L. Lu, W. heng Wu, Effect of welding speed on microstructure and mechanical properties of laser-welded transformation induced plasticity (TRIP) steels, J. Iron Steel Res. Int. 27 (2020) 1087–1098, https://doi.org/10.1007/S42243-020-00397-X.
[14] S.S. Nayak, V.H. Baltazar Hernandez, Y. Okita, Y. Zhou, Microstructure–hardness relationship in the fusion zone of TRIP steel welds, Mater. Sci. Eng. A. 551 (2012) 73–81, https://doi.org/10.1016/J.MSEA.2012.04.096.
[15] A. Grajcar, M. Morawiec, M. Różański, S. Stano, Twin-spot laser welding of advanced high-strength multiphase microstructure steel, Opt Laser. Technol. 92 (2017) 52–61, https://doi.org/10.1016/j.optlastec.2017.01.011.
[16] Q. Lang, X. Zhang, G. Song, L. Liu, Effects of different laser power and welding speed on the microstructure and mechanical properties of TRIP joints in laser-TIG arc hybrid lap filler wire welding, Mater. Today Commun. 29 (2021), https://doi.org/10.1016/J.MTCOMM.2021.102925.
[17] L. Cretteur, High-power beam welding of advanced high-strength steels (AHSS), Weld. Join. Adv. High Strength Steels (2015) 93–119, https://doi.org/10.1016/B978-0-85709-436-0.00006-0.
[18] Y. Wu, Y. Guo, W. Zhang, L. Li, Microstructure evolution and dynamic mechanical behavior of laser welded dissimilar joint between QP1180 and TRIP780, J. Mater. Res. Technol. 16 (2022) 977–987, https://doi.org/10.1016/J.JMRT.2021.12.076.
[19] R.S. Sharma, P. Molian, Yb:YAG laser welding of TRIP780 steel with dual phase and mild steels for use in tailor welded blanks, Mater. Des. 30 (2009) 4146–4155, https://doi.org/10.1016/J.MATDES.2009.04.033.
[20] L. Mujica, S. Weber, H. Pinto, C. Thomy, F. Vollertsen, Microstructure and mechanical properties of laser-welded joints of TWIP and TRIP steels, Mater. Sci. Eng. A. 527 (2010) 2071–2078, https://doi.org/10.1016/J.MSEA.2009.11.050.
[21] M. Rossini, P.R. Spena, L. Cortese, P. Matteis, D. Firrao, Investigation on dissimilar laser welding of advanced high strength steel sheets for the automotive industry, Mater. Sci. Eng. A. 628 (2015) 288–296, https://doi.org/10.1016/J.MSEA.2015.01.037.
[22] S. Erzincanlioğlu, T. Aydiner, F. Aras, H. Çelik, E. Billur, S. Karabulut, I.O. Gümüs, Development of new vehicle safety structures by using third-generation steels, SAE Int. J. Mater. Manuf. 15 (2022), https://doi.org/10.4271/05-15-02-0011.
[23] C.P. Kohar, M. Cherkaoui, H. El Kadiri, K. Inal, Numerical modeling of TRIP steel in axial crashworthiness, Int. J. Plast. 84 (2016) 224–254, https://doi.org/10.1016/J.IJPLAS.2016.05.010.

[24] A.S. Hamada, P. Sahu, D.A. Porter, Indentation property and corrosion resistance of electroless nickel-phosphorus coatings deposited on austenitic high-Mn TWIP steel, Appl. Surf. Sci. 356 (2015) 1–8, https://doi.org/10.1016/j.apsusc.2015.07.153.
[25] A. Monsalve, A. Guzmán, F. De Barbieri, A. Artigas, L. Carvajal, O. Bustos, N. F. Garza-Montes-de Oca, R. Colás, Mechanical and microstructural characterization of an aluminum bearing trip steel, Metall. Mater. Trans. A Phys. Metall. Mater. Sci. 47 (2016) 3088–3094, https://doi.org/10.1007/S11661-016-3435-5/FIGURES/10.
[26] H. Kong, Q. Chao, M.H. Cai, E.J. Pavlina, B. Rolfe, P.D. Hodgson, H. Beladi, Microstructure Evolution and Mechanical Behavior of a CMnSiAl TRIP Steel Subjected to Partial Austenitization Along with Quenching and Partitioning Treatment, Metall. Mater. Trans. A. 49 (n.d.). https://doi.org/10.1007/s11661-018-4525-3.
[27] P. Sahu, A.S. Hamada, T. Sahu, J. Puustinen, T. Oittinen, L.P. Karjalainen, Martensitic transformation during cold rolling deformation of an austenitic Fe-26Mn-0.14C alloy, Metall. Mater. Trans. A Phys. Metall. Mater. Sci. 43 (2012) 47–55, https://doi.org/10.1007/S11661-011-0818-5/FIGURES/6.
[28] A. Hamada, M. Ali, S. Ghosh, M. Jaskari, M. Keskitalo, A. Järvenpää, Mechanical performance and formability of laser-welded dissimilar butt joints between medium-Mn stainless steel and high-strength carbon steel, Mater. Sci. Eng. A. 831 (2022), 142200, https://doi.org/10.1016/J.MSEA.2021.142200.
[29] M. Hietala, M. Ali, A. Khosravifard, M. Keskitalo, A. Jarvenpaa, A. Hamada, Optimization of the tensile-shear strength of laser-welded lap joints of ultra-high strength abrasion resistance steel, J. Mater. Res. Technol. 11 (2021) 1434–1442, https://doi.org/10.1016/J.JMRT.2021.01.121.
[30] A.J. DeArdo, C.I. Garcia, K. Cho, M. Hua, New method of characterizing and quantifying complex microstructures in steels, Mater. Manuf. Process. 25 (2010) 33–40, https://doi.org/10.1080/10426910903143415.
[31] S. Morito, H. Yoshida, T. Maki, X. Huang, Effect of block size on the strength of lath martensite in low carbon steels, Mater. Sci. Eng. A. 438–440 (2006) 237–240, https://doi.org/10.1016/J.MSEA.2005.12.048.
[32] H. Kong, Q. Chao, B. Rolfe, H. Beladi, One-step quenching and partitioning treatment of a tailor welded blank of boron and TRIP steels for automotive applications, Mater. Des. 174 (2019), 107799, https://doi.org/10.1016/J.MATDES.2019.107799.
[33] M. Xia, Z. Tian, L. Zhao, Y.N. Zhou, Fusion zone microstructure evolution of Al-alloyed TRIP steel in diode laser welding, Mater. Trans. 49 (2008) 746–753, https://doi.org/10.2320/MATERTRANS.MRA2007271.
[34] A. Hamada, S. Ghosh, M. Ali, M. Jaskari, A. Järvenpää, Studying the strengthening mechanisms and mechanical properties of dissimilar laser-welded butt joints of medium-Mn stainless steel and automotive high-strength carbon steel, Mater. Sci. Eng. A. 856 (2022), 143936, https://doi.org/10.1016/J.MSEA.2022.143936.
[35] L.S. Derevyagina, A.I. Gordienko, Orishich, A.G. Malikov, N.S. Surikova, M. N. Volochaev, Microstructure of intercritical heat affected zone and toughness of microalloyed steel laser welds, Mater. Sci. Eng. A. 770 (2020), 138522, https://doi.org/10.1016/J.MSEA.2019.138522.
[36] A. Chatterjee, D. Chakrabarti, A. Moitra, R. Mitra, A.K. Bhaduri, Effect of normalization temperatures on ductile-brittle transition temperature of a modified 9Cr-1Mo steel, Mater. Sci. Eng. A. 618 (2014) 219–231, https://doi.org/10.1016/J.MSEA.2014.09.021.
[37] B.C. De Cooman, J.G. Speer, I.Y. Pyshmintsev, N. Yoshinaga, Materials Design, the Key of Modern Steel Products, Grips Media, Germany, 2007.
[38] H. Kitahara, R. Ueji, N. Tsuji, Y. Minamino, Crystallographic features of lath martensite in low-carbon steel, Acta Mater. 54 (2006) 1279–1288, https://doi.org/10.1016/J.ACTAMAT.2005.11.001.
[39] M. Amirthalingam, M. Hermans, I. Richardson, Microstructural development during welding of silicon and aluminum-based transformation-induced plasticity steels-inclusion and elemental partitioning analysis, Metall. Mater. Trans. A Phys. Metall. Mater. Sci. 40 (2009) 901–909, https://doi.org/10.1007/s11661-008-9761-5.
[40] K. Dilger, S. Kreling, Welding and joining of advanced high strength steels (AHSS). http://www.sciencedirect.com:5070/book/9780857094360/welding-and-joining-of-advanced-high-strength-steels-ahss, 2015. (Accessed 11 May 2023).
[41] J. Teixeira, M. Moreno, S.Y.P. Allain, C. Oberbillig, G. Geandier, F. Bonnet, Intercritical annealing of cold-rolled ferrite-pearlite steel: microstructure evolutions and phase transformation kinetics, Acta Mater. 212 (2021), 116920, https://doi.org/10.1016/j.actamat.2021.116920.
[42] A. Chbihi, D. Barbier, L. Germain, A. Hazotte, M. Gouné, Interactions between ferrite recrystallization and austenite formation in high-strength steels, J. Mater. Sci. 49 (2014) 3608–3621, https://doi.org/10.1007/S10853-014-8029-2/FIGURES/13.
[43] L.S. Thomas, D.K. Matlock, Formation of banded microstructures with rapid intercritical annealing of cold-rolled sheet steel, Metall. Mater. Trans. A Phys. Metall. Mater. Sci. 49 (2018) 4456–4473, https://doi.org/10.1007/s11661-018-4742-9.
[44] C. Zheng, D. Raabe, D. Li, Prediction of post-dynamic austenite-to-ferrite transformation and reverse transformation in a low-carbon steel by cellular automaton modeling, Acta Mater. 60 (2012) 4768–4779, https://doi.org/10.1016/j.actamat.2012.06.007.
[45] H. Dong, Y. Zhang, G. Miyamoto, M. Inomoto, H. Chen, Z. Yang, T. Furuhara, Unraveling the effects of Nb interface segregation on ferrite transformation kinetics in low carbon steels, Acta Mater. 215 (2021), 117081, https://doi.org/10.1016/j.actamat.2021.117081.
[46] A. Hamada, T. Juuti, A. Khosravifard, A. Kisko, P. Karjalainen, D. Porter, J. Kömi, Effect of silicon on the hot deformation behavior of microalloyed TWIP-type stainless steels, Mater. Des. 154 (2018) 117–129, https://doi.org/10.1016/J.MATDES.2018.05.029.
[47] W. Lu, M. Herbig, C.H. Liebscher, L. Morsdorf, R.K.W. Marceau, G. Dehm, D. Raabe, Formation of eta carbide in ferrous martensite by room temperature aging, Acta Mater. 158 (2018) 297–312, https://doi.org/10.1016/J.ACTAMAT.2018.07.071.
[48] P. Kaikkonen, S. Ghosh, M. Somani, J. Kömi, Nanostructured bainite transformation characteristics in medium-carbon steel subjected to ausforming and isothermal holding below martensite start temperature, J. Mater. Res. Technol. 23 (2023) 466–490, https://doi.org/10.1016/J.JMRT.2023.01.002.
[49] S. Ghosh, P. Kaikkonen, V. Javaheri, A. Kaijalainen, I. Miettunen, M. Somani, J. Kömi, S. Pallaspuro, Design of tough, ductile direct quenched and partitioned advanced high-strength steel with tailored silicon content, J. Mater. Res. Technol. 17 (2022) 1390–1407, https://doi.org/10.1016/J.JMRT.2022.01.073.
[50] I. Miettunen, S. Ghosh, M.C. Somani, S. Pallaspuro, J. Kömi, Competitive mechanisms occurring during quenching and partitioning of three silicon variants of 0.4 wt.% carbon steels, J. Mater. Res. Technol. 11 (2021) 1045–1060, https://doi.org/10.1016/J.JMRT.2021.01.085.
[51] S. Ghosh, K. Rakha, A. Aravindh, S. Devi, S. Reza, S. Pallaspuro, M. Somani, M. Huttula, J. Kömi, A combined 3D-atomic/nanoscale comprehension and ab initio computation of iron carbide structures tailored in Q&P steels via Si alloying, Nanoscale (2023), https://doi.org/10.1039/D3NR00816A.
[52] A. Dhal, S.K. Panigrahi, M.S. Shunmugam, Achieving excellent microformability in aluminum by engineering a unique ultrafine-grained microstructure, Sci. Rep. 9 (2019) 1–13, https://doi.org/10.1038/s41598-019-46957-4.
[53] P.J. Jacques, E. Girault, A. Mertens, B. Verlinden, J. Van Humbeeck, F. Delannay, The developments of cold-rolled TRIP-assisted multiphase steels. Al-Alloyed TRIP-assisted multiphase steels, ISIJ Int. 41 (2001) 1068–1074, https://doi.org/10.2355/ISIJINTERNATIONAL.41.1068.
[54] J. Akré, F. Danoix, H. Leitner, P. Auger, The morphology of secondary-hardening carbides in a martensitic steel at the peak hardness by 3DFIM, Ultramicroscopy 109 (2009) 518–523, https://doi.org/10.1016/J.ULTRAMIC.2008.11.010.
[55] J.H. Zhou, Y.F. Shen, Y.Y. Hong, W.Y. Xue, R.D.K. Misra, Strengthening a fine-grained low activation martensitic steel by nanosized carbides, Mater. Sci. Eng. A. 769 (2020), 138471, https://doi.org/10.1016/J.MSEA.2019.138471.
[56] A. Kulkarni, D.K. Dwivedi, M. Vasudevan, Microstructure and mechanical properties of A-TIG welded AISI 316L SS-Alloy 800 dissimilar metal joint, Mater. Sci. Eng. A. 790 (2020), 139685, https://doi.org/10.1016/j.msea.2020.139685.
[57] N. Dimov, D. Weisz-Patrault, A. Tanguy, T. Sapanathan, J. Benoist, E. Charkaluk, A. Simar, Strain and damage analysis using high resolution digital image correlation in the stir zone of an AA6061-AA7075 dissimilar friction stir weld, Mater. Today Commun. 34 (2023), 105359, https://doi.org/10.1016/j.mtcomm.2023.105359.
[58] T. Wang, R. Mishra, Effect of stress concentration on strength and fracture behavior of dissimilar metal joints, in: Miner. Met. Mater. Ser., Springer International Publishing, 2019, pp. 33–39, https://doi.org/10.1007/978-3-030-05752-7_4.
[59] Y. Uematsu, T. Kakiuchi, K. Niimi, P.D.T. Caiza, Local strain analysis under quasi-static tensile loading in Al/steel dissimilar friction stir weld by a digital image correlation method, Int. J. Adv. Manuf. Technol. 120 (2022) 349–360, https://doi.org/10.1007/s00170-021-08481-6.